

Quantum scars of bosons with correlated hopping

Ana Hudomal,¹ Ivana Vasić,¹ Nicolas Regnault,^{2,3} and Zlatko Papić⁴

¹*Scientific Computing Laboratory, Center for the Study of Complex Systems, Institute of Physics Belgrade, University of Belgrade, 11080 Belgrade, Serbia*

²*Joseph Henry Laboratories and Department of Physics, Princeton University, Princeton, New Jersey 08544, USA*

³*Laboratoire de Physique de l'École Normale Supérieure, ENS, Université PSL, CNRS, Sorbonne Université,*

Université Paris-Diderot, Sorbonne Paris Cité, 75005 Paris, France

⁴*School of Physics and Astronomy, University of Leeds, Leeds LS2 9JT, United Kingdom*

(Dated: October 22, 2019)

Recent experiments have shown that preparing an array of Rydberg atoms in a certain initial state can lead to unusually slow thermalization and persistent density oscillations [Bernien *et al.*, Nature **551**, 579 (2017)]. This type of non-ergodic behavior has been attributed to the existence of “quantum many-body scars”, i.e., atypical eigenstates of a system that have high overlaps with a small subset of vectors in the Hilbert space. Periodic dynamics and many-body scars are believed to originate from a “hard” kinetic constraint: due to strong interactions, no two neighbouring Rydberg atoms are both allowed to be excited. Here we propose a realization of quantum many-body scars in a 1D bosonic lattice model with a “soft” constraint: there are no restrictions on the allowed boson states, but the amplitude of a hop depends on the occupancy of the hopping site. We find that this model exhibits similar phenomenology to the Rydberg atom chain, including weakly entangled eigenstates at high energy densities and the presence of a large number of exact zero energy states, with distinct algebraic structure. We discuss the relation of this model to the standard Bose-Hubbard model and possible experimental realizations using ultracold atoms.

I. INTRODUCTION

Semiclassical studies of chaotic stadium billiards have revealed the existence of remarkable non-chaotic eigenfunctions called *quantum scars*.¹ Scarred eigenfunctions display anomalous enhancement in regions of the billiard that are traversed by one of the periodic orbits in the classical limit when $\hbar \rightarrow 0$. It was shown that quantum scars lead to striking experimental signatures in a variety of systems, including microwave cavities,² quantum dots,³ and semiconductor quantum wells.⁴

A recent experiment on a quantum simulator,⁵ and subsequent theoretical work,^{6,7} have shown that quantum *many-body* scars can occur in strongly interacting quantum systems. The experiment used a one-dimensional Rydberg atom platform^{5,8,9} in the regime of the Rydberg blockade, where nearest-neighbour excitations of the atoms were energetically prohibited. The experiment observed persistent many-body revivals of local observables after a “global quench”¹⁰ from a certain initial state. In contrast, when the experiment was repeated for other initial configurations, drawn from the same type of “infinite” temperature ensemble, the system displayed fast equilibration and no revivals. These observations pointed to a different kind of out-of-equilibrium behaviour compared to previous studies of quantum thermalization in various experimental platforms.^{11–15}

In both single-particle and many-body quantum scars, the dynamics from certain initial states leads to periodic revivals of the wave function. In the former case, this happens when the particle is prepared in a Gaussian wave packet initialized along a periodic orbit. In

the latter case, the Rydberg atoms are prepared in a Néel product state, where every second atom is excited. The collective dynamics from such an initial state was shown to be effectively “semiclassical”,⁷ i.e., it is effectively restricted to a subset of the Hilbert space and can be interpreted as a nearly-free precession of an emergent spin-1/2 degree of freedom.¹⁶

Another similarity between single- and many-body quantum scars is the presence of non-ergodic eigenstates. As mentioned above, in the single-particle case, such eigenstates are easily identified by their non-uniform probability density that sharply concentrates along classical periodic orbits. In the many-body case, non-ergodic eigenstates are broadly defined as those that violate Eigenstate Thermalization Hypothesis (ETH).^{17,18} In the Rydberg atom chain describing Ref. 5, such eigenstates appear at evenly spaced energies throughout the spectrum of the system.^{6,19,20} Scarred eigenstates violate the ETH in a number of ways: for example, they have anomalous expectation values of local observables compared to other eigenstates at the same energy density, and their entanglement entropy obeys a sub-volume law scaling,¹⁹ i.e., scarred eigenstates are weakly entangled compared to random vectors in the many-body Hilbert space.

In recent works, the existence of atypical eigenstates has been taken as a more general definition of quantum many-body scarring. For example, highly-excited eigenstates with low entanglement have previously been analytically constructed in the non-integrable AKLT model.^{21,22} A few of such exact eigenstates are now also available for the Rydberg atom chain model.²³ The collection of models that feature atypical eigen-

states is rapidly expanding, including perturbations of the Rydberg atom chain,^{19,24,25} theories with confinement,^{26–28} Fermi-Hubbard model beyond one dimension,^{29,30} driven systems,³¹ fractional quantum Hall effect in a one-dimensional limit,³² and models with fracton-like dynamics.^{33–36} In a related development, it was proposed that atypical eigenstates of one Hamiltonian can be “embedded” into the spectrum of another, thermalizing Hamiltonian,³⁷ causing a violation of a “strong” version of the ETH.^{38,39} This approach allows to engineer scarred eigenstates in models of topological phases in arbitrary dimensions.⁴⁰ From a dynamical point of view, it has been shown that models with scarred dynamics can be systematically constructed by embedding periodic on-site unitary dynamics into a many-body system.⁴¹

A feature shared by the models currently believed to support quantum many-body scars is the presence of some form of a *kinetic constraint*. In the Rydberg atom chain, the constraint results from strong van der Waals forces between neighbouring excitations. Formally, this means that all configurations with adjacent Rydberg excitations are removed from the low-energy subspace. The resulting effective Hilbert space, while still exponentially large in the number of atoms, is no longer a tensor product of two-level systems.⁴² Such Hilbert spaces occur, for example, in models describing anyon excitations in topological phases of matter^{43–45} due to a global constraint imposed by an emergent gauge field. Recent numerical investigations of the ETH in such models have argued that they generically thermalize.^{46,47} Kinetic constraints emerge naturally in models of lattice gauge theories,^{48–50} including the Rydberg atom system.^{51,52} Recent works on periodically driven optical lattices have started to explore such physics.^{53,54}

On the other hand, kinetic constraints have been investigated as a possible pathway to many-body localization without disorder.⁵⁵ In classical systems, non-thermalizing behavior without disorder is well-known in the context of structural glasses.^{56–58} The mechanism of this type of behavior is the excluded volume interactions that impose kinetic constraints on the dynamics.^{59,60} Similar type of physics has recently been explored in quantum systems where a “quasi many-body localized” behavior was proposed to occur in the absence of disorder.^{61–71} In this paper we address the question of the relation between kinetic constraint, slow dynamics and quantum many-body scars. In contrast to previous work, which primarily focused on spins and fermions that are closely related in one dimension, we study kinetically-constrained models of bosons in one-dimension.

This paper is organized as follows. In Sec. II we introduce the models of bosons with correlated hopping and discuss properties of their Hamiltonians when viewed as adjacency matrices of graphs in the Fock space. In Sec. III we investigate thermalization properties of these models by studying their energy level statistics, entanglement entropy of eigenstates, and dynamics under global quench. In Sec. IV we identify initial states that give rise

to periodic many-body revivals in the quantum dynamics, and we introduce a “cluster approximation” that captures the scarred eigenstates that are responsible for such periodic revivals. Finally, our conclusions and a discussion of experimental realizations is presented in Sec. V.

II. MODELS AND THEIR HILBERT SPACES

A fundamental ingredient of kinetically constrained models is “correlated hopping”: a particle can hop depending on the state of its neighbors. In this paper we consider a system of N_p bosons on a one-dimensional lattice with L sites. We consider models where the total filling factor, $\nu = N_p/L$, is conserved, and we will mainly present results in the dense regime, $\nu = 1$. We have studied models with $\nu < 1$ and $\nu > 1$, but we found them to be either too constrained or not constrained enough, and therefore less interesting. We emphasize that the bosons in our study are *not* hard-core, i.e., the occupancy of any lattice site can take any value from 0 to N_p .

A. Models

We study three different models, defined by the Hamiltonians:

$$H_1 = -J \sum_{j=1}^L \left(b_j^\dagger b_{j+1} n_j + n_{j-1} b_j^\dagger b_{j-1} \right), \quad (1)$$

$$H_2 = -J \sum_{j=1}^L \left(n_j b_j^\dagger b_{j+1} + b_j^\dagger b_{j-1} n_{j-1} \right), \quad (2)$$

$$H_3 = -J \sum_{j=1}^L \left(n_{j+1} b_j^\dagger b_{j+1} n_j + n_{j-1} b_j^\dagger b_{j-1} n_j \right). \quad (3)$$

All three models contain a free-boson hopping term, $b_j^\dagger b_{j+1}$, which is dressed in various ways by density operators, $n_j = b_j^\dagger b_j$. We will show that the position of the density operator n_j completely changes the behavior of these models, ranging from fast thermalization to the breakup of the Hamiltonian into disconnected, exactly solvable sectors. For example, note that H_1 and H_2 are related to each other via free boson hopping,

$$H_2 = H_1 - J \sum_j \left(b_j^\dagger b_{j+1} + b_j^\dagger b_{j-1} \right), \quad (4)$$

which can be easily proven using bosonic commutation relations. We will see below that this innocuous free-boson hopping leads to surprisingly different dynamical properties of the two models.

The motivation behind introducing three different models in Eqs. (1)-(3) can be summarized as follows. Hamiltonian H_1 describes a model where a particle cannot hop to the left if that site is not already occupied by at least one particle, and cannot hop to the right if

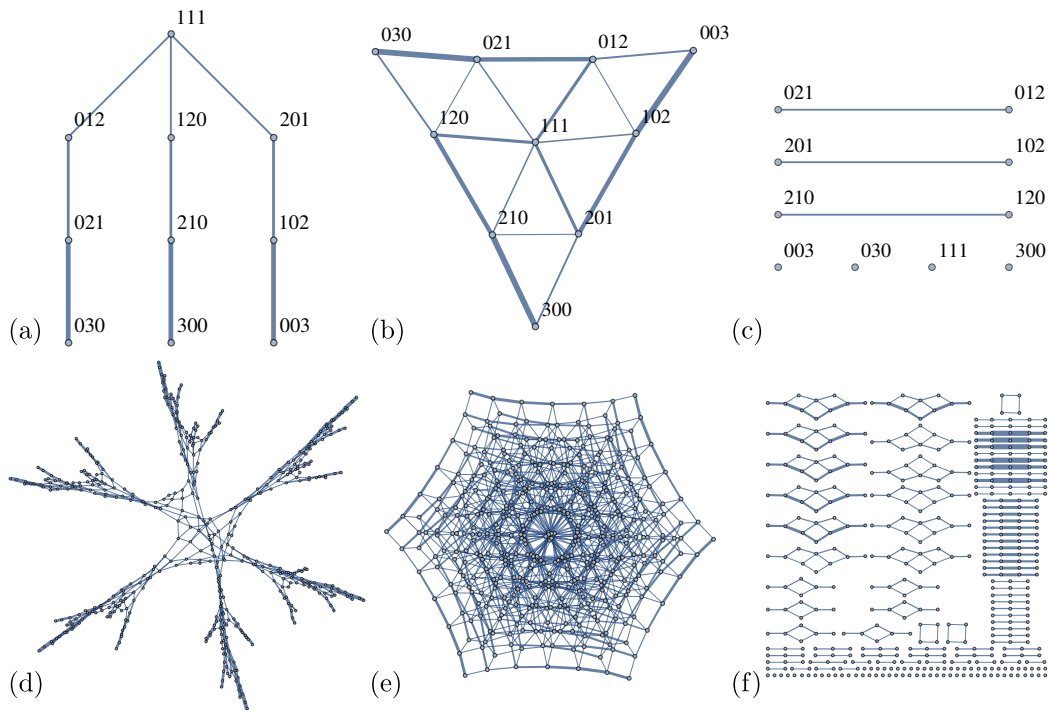


Figure 1. Connectivity of the Hilbert space for the three models defined in Eqs. (1)-(3). Top row: adjacency graph for (a) H_1 , (b) H_2 , (c) H_3 , all for $L = N_p = 3$. Bottom row: same as top but for $L = N_p = 6$. To avoid clutter, we do not label the vertices in (d), (e) and (f). All graphs are weighted, i.e., the line thickness is proportional to the magnitude of the corresponding hopping coefficient. Several different clusters of configurations are visible in the case of H_1 . The clusters start to form already for $L = 3$ (for example, the configurations 012–021–003 in (a)) and become more prominent for $L = 6$ (d). In the case of H_2 , almost all configurations are well-connected to the rest of the graph. The graphs for H_3 show that the Hilbert space is highly reducible: its graph splits into many disconnected components.

it is the only particle left on its initial site. This introduces constraints to the system. Conversely, there are no such constraints in the case of H_2 . Indeed, the hopping coefficients are only modified in intensity by the particle-number operator. Hamiltonian H_3 introduces additional constraints compared to H_1 . The number of unoccupied sites and their positions remain constant under the action of this Hamiltonian. This leads to different connectivity of the Hilbert space in each of the models, as we explain in Sec. II B.

We consider periodic boundary conditions ($L + 1 \equiv 1$) and set $\hbar = J = 1$. With periodic boundary conditions, all three Hamiltonians H_1 , H_2 and H_3 have translation symmetry, thus their eigenstates can be labelled by momentum quantum number, k , quantized in units of $2\pi/L$. In addition, H_3 has inversion symmetry. We denote by $I = 0$ and $I = 1$ the sectors that are even and odd under inversion, respectively.

Without restrictions on the boson occupancy, the Hilbert space of H_1 , H_2 and H_3 grows very rapidly. For $L = N_p = 12$, the Hilbert space size of the $k = 0$ sector is 112720 (the largest one we will consider for H_1 and H_2). As previously mentioned (see also Sec. II B below), the Hilbert space of H_3 splits into many disconnected components, thus it is possible to consider only one connected component at a time and disregard the unoccupied sites

whose positions do not change. This is more relevant when looking at properties such as thermalization, than fixing the filling factor. However, the boundary conditions are in that case no longer periodic, and the system does not have translation symmetry. Considering only a system with the size $L/2$, filling factor $\nu = 2$, open boundary conditions and minimal number of particles per site equal to 1 is completely equivalent to considering the largest component of the full system which has the size L , filling factor $\nu = 1$, periodic boundary conditions and no restrictions on the occupancies. The Hilbert space size of the symmetric invariant sector of the largest connected component of $L = N_p = 22$ is 176484 and this is the largest sector that we will consider for H_3 .

B. Graph structure and bipartite lattice

Since we will be interested in the dynamical properties, it is convenient to first build some intuition about the structure of the Hamiltonians of the three models in Eqs. (1)-(3). A Hamiltonian can be viewed as the adjacency matrix of a graph whose vertices are Fock states of bosons, $|n_1, n_2, \dots, n_L\rangle$. If the Hamiltonian induces a transition between two Fock states, the corresponding vertices of the graph are connected by a link. The graphs

that show how the configuration space is connected have very different structure for the three Hamiltonians H_1 , H_2 and H_3 , as can be observed in Fig. 1.

The entire graph of H_2 is well-connected and it has the same structure as the graph of the standard Bose-Hubbard model: the particle-number operators in H_2 do not introduce any constraints, but only affect the magnitude of the hopping coefficients. In contrast, the H_1 graph shows several clusters of configurations that are weakly connected to the rest of the graph. “Weakly connected” means that there is a small number of connections leading outside the cluster and that their respective hopping coefficients are smaller in magnitude than those of the surrounding connections within the cluster. A state that is initially located inside a cluster is therefore more likely to stay inside during an initial stage of the time evolution, which increases the probability of revivals and slows down the growth of entanglement entropy. We will provide a more quantitative description and examples that illustrate this in Sec. IV. Finally, the graph of H_3 , due to even stronger constraints, is actually disconnected. This predicts that thermalization and dynamics in the three models will be very different, which we will confirm in Section III. However, we note that the number of connections and the topology of the graph is not the only relevant factor for the dynamics. The magnitude of the hopping coefficients between different configurations is also important, which is discussed in Appendix A.

We note that the relation between H_1 and H_3 is reminiscent of the relation between the quantum East model⁷² and the “PXP” model describing the atoms in the Rydberg blockade regime.^{6,19,42} Like H_3 , the PXP model is doubly constrained and inversion symmetric, while H_1 and the quantum East model are asymmetric versions of those two models with only a single constraint. The graph of the quantum East model is similar to that of H_1 , in that it contains bottlenecks which slow down the growth of entanglement entropy.⁷²

Hamiltonian H_1 has a bipartite structure, i.e. all the basis configurations can be divided into two disjoint sets, and the action of the Hamiltonian connects configurations in one set only to the configurations in the other and vice-versa (the Hamiltonian is off-diagonal). One way to sort configurations into these two sets is by parity of the quantity

$$\Delta_a = \frac{|n_{\text{even}} - n_{\text{odd}}|}{2}. \quad (5)$$

We define n_{even} and n_{odd} as the total numbers of particles at even and odd sites respectively

$$n_{\text{even}} = \sum_{l=1}^{L_1} n_{2l}, \quad n_{\text{odd}} = \sum_{l=1}^{L_2} n_{2l-1}, \quad (6)$$

where $L_1 = L_2 = L/2$ if L is even, and $L_1 = (L-1)/2$, $L_2 = (L+1)/2$ if L is odd. If only nearest neighbor hoppings are allowed and if no two odd sites are coupled (if the system has open boundary conditions for any L or

periodic boundary conditions for L -even), each hopping either increases n_{even} by one and decreases n_{odd} by one, or vice-versa. This means that each hopping can change Δ_a only by ± 1 .

In special cases like H_1 at filling factor $\nu = 1$ it is also possible to define quantities like Δ_a for odd system sizes and periodic boundary conditions. This is a consequence of the constraints imposed by H_1 , i.e., the fact that a particle cannot hop to an empty site to its left (see Appendix B). Note that H_2 in the same geometry is not bipartite.

Another way to sort configurations into two sets is by parity of the distance from the configuration $|111\dots 111\rangle$, which we define as

$$d_a = \min_n \{ \langle 111\dots 111 | H_1^n | a \rangle \neq 0 \}. \quad (7)$$

In this case, the two sets are the configurations with even and with odd distances d_a . One hopping can change d_a only by ± 1 or 0. Changes by other values are not possible by definition if the Hamiltonian is Hermitian (all hoppings are reversible). Both d_a and Δ_a have the same parity, thus d_a must always change after one hopping in even system sizes or in systems with open boundary conditions. As a consequence, d_a cannot change by 0 if Δ_a can only change by ± 1 .

The graphs of bipartite systems do not contain any loops of odd dimension (triangles, pentagons, heptagons and so on). Moreover, the energy spectra of bipartite systems are symmetric around zero. Their Hamiltonians anticommute with the operator $(-1)^{\Delta_a}$. The presence of such an operator in a bipartite lattice leads to exact zero energy states in the spectrum.^{73,74} We discuss in detail this zero-energy manifold in Appendix C.

III. DYNAMICS AND ENTANGLEMENT PROPERTIES

We now investigate the phenomenology of the models introduced in Eqs. (1)-(3). We use full exact diagonalization to obtain the complete set of energy eigenvalues and eigenvectors, from which we evaluate the level statistics and the distribution of entanglement entropies for the three models. Furthermore, we probe dynamical properties of the models by studying a global quench, simulated via Krylov iteration.

A. Level statistics and entanglement entropy

The energy level statistics is a standard test for thermalization of models that cannot be solved exactly. A convenient way to probe the level statistics is to examine the probability distribution $P(r)$ ⁷⁵ of ratios between consecutive energy gaps $s_n = E_{n+1} - E_n$,

$$r = \frac{\min(s_n, s_{n+1})}{\max(s_n, s_{n+1})}. \quad (8)$$

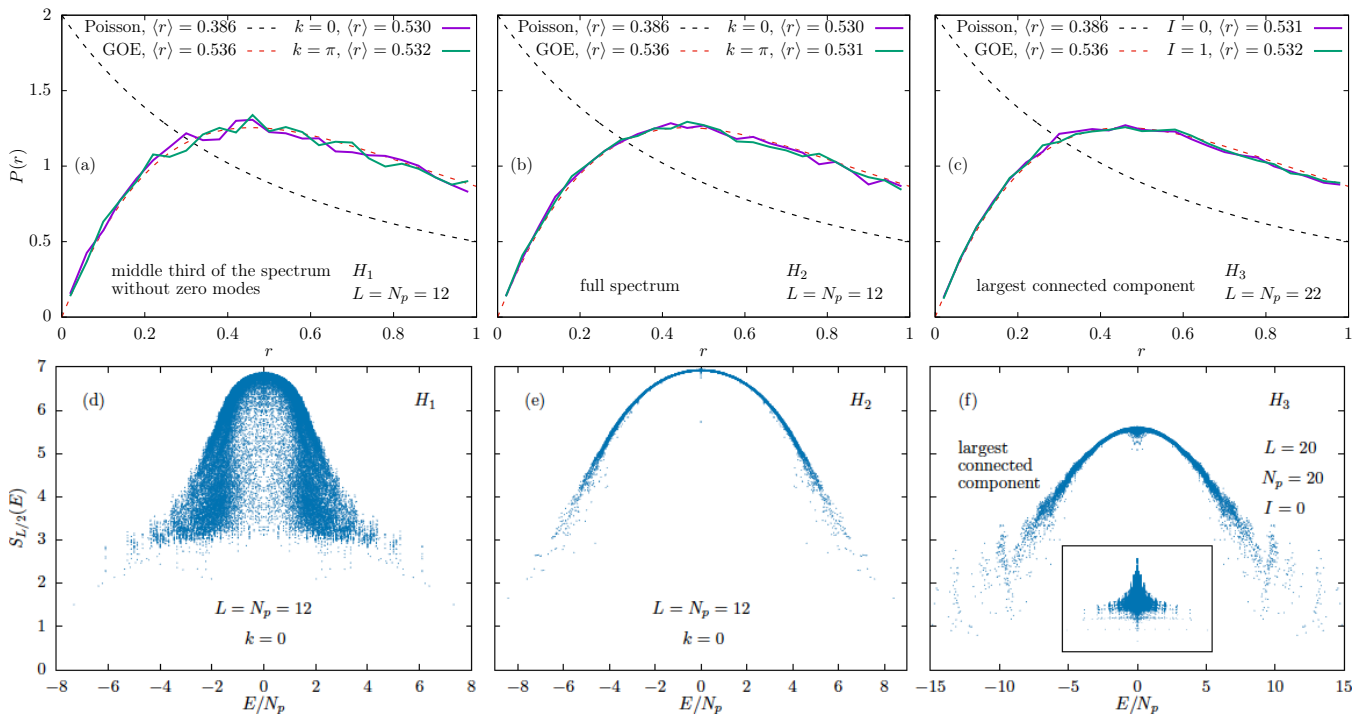


Figure 2. Top row: Probability distribution of the ratios of two consecutive energy gaps. (a) H_1 (middle third of the spectrum without $E = 0$ states, $L = N_p = 12$), (b) H_2 (full spectrum, $L = N_p = 12$) and (c) H_3 (largest connected component of $L = N_p = 22$). The black dashed line shows the Poisson distribution, which corresponds to the integrable case, while the red dashed line is the distribution of the Gaussian orthogonal ensemble, which corresponds to the thermalizing case. Bottom row: Entanglement entropies $S_{L/2}$ of all eigenstates plotted as a function of the eigenstate energy per particle, E/N_p . (d) H_1 ($L = N_p = 12$, $L_A = 6$, $k = 0$), (e) H_2 (same) and (f) H_3 in the largest connected component of $L = N_p = 20$, $L_A = 10$, $I = 0$. The inset shows all connected components for $L = N_p = 12$, $L_A = 6$, $k = 0$.

The advantage of studying $P(r)$, instead of $P(s_n)$, is that there is no need to perform the spectrum unfolding procedure – see Ref. 76. For standard random matrix theory ensembles, both $P(r)$ and the mean $\langle r \rangle$ are well-known.⁷⁷ When computing the same quantities in a microscopic physical model, it is crucial to resolve all the symmetries of the model.

The probability distribution $P(r)$ of the ratios of two consecutive energy gaps is shown in Figs. 2(a), (b) and (c) for the three Hamiltonians H_1 , H_2 and H_3 respectively, and two momentum or inversion sectors. In all three cases, the energy levels repel, i.e., the distribution tends to zero as $r \rightarrow 0$. For H_2 , the distribution is particularly close to the Wigner-Dyson (non-integrable) line. For H_1 , the distribution is also consistent with Wigner-Dyson when we restrict to the middle 1/3 of the spectrum (and after removing special states with $E = 0$ that we discuss in Appendix C). We exclude the edges of the spectrum because they contain degeneracies which are not symmetry-related. However, such states do not appear to have a major effect on the level statistics distribution, which is still closer to the Wigner-Dyson than the Poisson distribution even if they are included. The level statistics of H_3 within the largest connected component of the Hilbert space is shown in Fig. 2(c) and is also consistent with the Wigner-Dyson distribution without restricting

the spectrum. However, we will demonstrate below that the dynamics in some smaller connected components of H_3 can be exactly solved.

As a complementary diagnostic of thermalization, we next compute the entanglement entropy of all eigenstates. We divide the lattice into two sublattices, A and B , of lengths L_A and $L_B = L - L_A$. For a given pure state $|\psi\rangle$, the entanglement entropy is defined as

$$S_A = -\text{tr}_A(\rho_A \ln \rho_A), \quad (9)$$

where $\rho_A = \text{tr}_B |\psi\rangle\langle\psi|$ is the reduced density matrix of the subsystem A . The scatter plots, showing entanglement entropy of all eigenstates $|E_n\rangle$ as a function of their energy E_n , are displayed in Figs. 2(d), (e) and (f). Here we take into account the translation symmetry of the system and work in the momentum sector $k = 0$ for H_1 and H_2 , and consider only the largest connected component and the inversion sector $I = 0$ for H_3 . The results for other sectors are qualitatively similar.

Entanglement entropy distribution in Figs. 2(d) and (e) reveals a striking difference between the Hamiltonians H_1 and H_2 , even though they only differ by a free-boson hopping term, Eq. (4). The model H_1 is constrained, which leads to a large spread of the entropy distribution and many low-entropy eigenstates including in the bulk of the spectrum. From this perspective, H_1 is reminis-

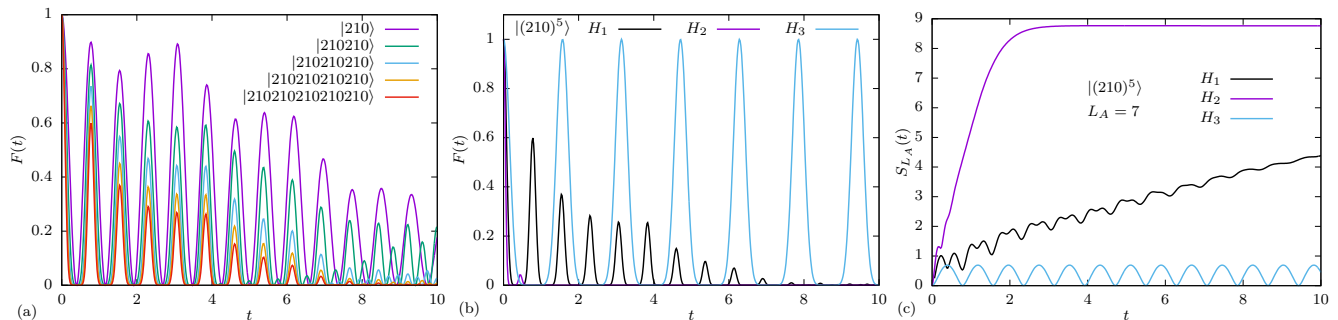


Figure 3. Dynamics of quantum fidelity and entanglement entropy for initial configurations of the form in Eq. (12). (a) Time evolution of fidelity $F(t)$ in Eq. (11) for system sizes $L = 3n$. The evolution is governed by the Hamiltonian H_1 , different colors represent different system sizes L . (b) Fidelity evolution $F(t)$ for the Hamiltonians H_1 , H_2 and H_3 and system size $L = 15$. (c) Entanglement entropy evolution $S_{L_A}(t)$ for the same cases as in (b).

cent of PXP model.^{19,24} By contrast, H_2 has no such constraints and in this case the entanglement entropy is approximately a smooth function of the eigenstate energy. The Hamiltonian H_3 is doubly constrained, and this is reflected in its entanglement distribution, which also shows a large spread and several disconnected bands, reminiscent of an integrable system like the XY model.⁷⁸

B. Global quenches

The constraints in the models in Eqs. (1), (2) and (3) have significant effects on the dynamics governed by these Hamiltonians. We probe the dynamics by performing a global quench on the system. We assume the system is isolated and prepared in one of the Fock states, $|\psi_0\rangle$, at time $t = 0$. We restrict to $|\psi_0\rangle$ being product states which are not necessarily translation-invariant, as such states are easier to prepare in experiment. However, our results remain qualitatively the same if we consider translation-invariant $|\psi_0\rangle$. After preparing the system in the state $|\psi_0\rangle$, which is not an eigenstate of the Hamiltonian, the system is let to evolve under unitary dynamics,

$$|\psi(t)\rangle = \exp\left(-\frac{i}{\hbar}Ht\right)|\psi_0\rangle. \quad (10)$$

where H is one of the Hamiltonians of interest. From the time-evolved state, we evaluate the quantum fidelity,

$$F(t) = |\langle\psi_0|\psi(t)\rangle|^2, \quad (11)$$

i.e., the probability for the wave function to return to the initial state. In a thermalizing system, fidelity decays rapidly to zero by the time $t^* \sim O(1/J)$ and remains exponentially suppressed at later times. In scarred models, such as the Rydberg atom chain,¹⁹ fidelity was found to revive to a finite fraction even at long times $t \gg 1/J$.

We first consider the Hamiltonian H_1 . Several configurations exhibit periodic revivals of the fidelity $F(t)$, which can in some cases be higher than 90%. Most of these configurations involve a very dense cluster of bosons such as

$|\dots 0N10\dots\rangle$. In contrast, a completely uniform configuration $|\dots 111\dots\rangle$ thermalizes very quickly. Here we focus on periodically-reviving configurations with density being as uniform as possible. One family of such reviving configurations involves n unit cells made of 3 lattice sites:

$$|210210\dots 210\rangle \equiv |(210)^n\rangle. \quad (12)$$

Time evolution of the fidelity for the initial state $|(210)^n\rangle$ for different system sizes $L = 3n$ is shown in Fig. 3(a). The initial state is assumed to be the product state, e.g., $|\psi_0\rangle = |210\rangle$ for $L = 3$. The frequency of the revivals in Fig. 3 is approximately the same for all system sizes. We emphasize that similar results are obtained for a translation-symmetric initial state, e.g., $|\psi_0\rangle = \frac{1}{\sqrt{3}}(|210\rangle + |021\rangle + |102\rangle)$. Both cases converge in the large system limit, and the differences are only significant for $L = 3$ when the revival frequency of the initial state with transition symmetry differs from the frequencies of other system sizes.

In Fig. 3(b) we compare the fidelity for the initial state in Eq. (12) when it is evolved by all three Hamiltonians in Eqs. (1)-(3). The initial state is fixed to be $|(210)^5\rangle$. We observe that the dynamics with H_3 has very prominent revivals; in fact as we will later show, these revivals are perfect and their period is approximately twice the revival period for H_1 . In contrast, for H_2 the fidelity quickly drops to zero without any subsequent revivals.

Finally, in Fig. 3(c) we plot the time evolution of entanglement entropy. As expected from the fast decay of the fidelity, the entropy for H_2 rapidly saturates to its maximal value. Moreover, as expected from the perfect revivals in H_3 , the entropy in that case oscillates around a constant value close to zero. For H_1 , we observe a relatively slow growth of entropy, with oscillations superposed on top of that growth, again similar to PXP model.⁶ For the initial state that is not translation-invariant, it is important how we cut the system, e.g., $|\dots 210|210\dots\rangle$ versus $|\dots 2102|10\dots\rangle$. In the first case, the entanglement entropy remains zero for H_3 because no particle can hop from one subsystem to the other, while in the second case the entropy oscillates around a con-

stant value, which is the case in Fig. 3(c).

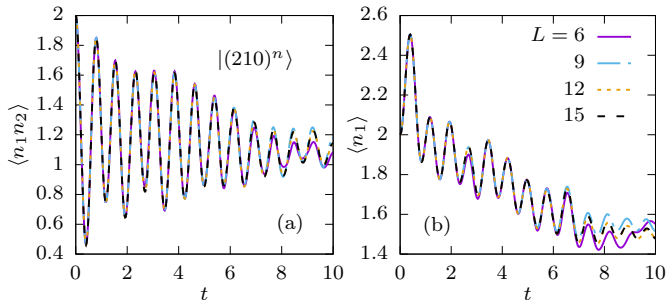


Figure 4. Evolution of (a) correlations between adjacent sites $\langle n_1 n_2(t) \rangle$ and (b) density on one site $\langle n_1(t) \rangle$ for different system sizes and the initial state $|(210)^n$.

In Fig. 4 we show the evolution of two local observables, density correlations between two adjacent sites $\langle n_1 n_2(t) \rangle$ and density on the first site $\langle n_1(t) \rangle$, starting from the initial state $|(210)^n$. Unlike fidelity and entanglement entropy, these observables can be easily measured in experiment. Both observables robustly oscillate with approximately the same frequency as the fidelity. The heights of the first few revival peaks are approximately converged for the system sizes ranging from $L = 6$ to $L = 15$, which suggests that revivals in such local observables can be observed in the thermodynamic limit. In the following Section, we will show that the oscillations observed in the dynamics from $|(210)^n$ state and their frequency can be explained using a tractable model that involves only a small subset of all configurations in the Hilbert space, thus providing a realization of quantum scars in a correlated bosonic system.

IV. PERIODIC REVIVALS

In this Section, we introduce a toy model that explains the dynamics and predicts the frequency of revivals in H_1 from the initial state $|(210)^n$ in Eq. (12). Our starting point will be the model H_3 , whose graph explicitly separates into disconnected subsets which makes the toy model exact, hence we can analytically calculate the revival frequency. Based on these results, we then introduce an approximation scheme that describes the dynamics from the same initial state under the H_1 Hamiltonian.

A. H_3 model: Perfect revivals

We start with a warmup calculation for H_3 acting on $L = 3$ sites. The connected subspace of 210 contains only two configurations, 120 and 210. The Hamiltonian reduced to this subspace is

$$H'_3 = - \begin{pmatrix} 0 & 2 \\ 2 & 0 \end{pmatrix}, \quad (13)$$

where the basis vectors are

$$\begin{pmatrix} 1 \\ 0 \end{pmatrix} = |210\rangle, \quad \begin{pmatrix} 0 \\ 1 \end{pmatrix} = |120\rangle. \quad (14)$$

The eigenvalues of H'_3 are $E_1 = -2$ and $E_2 = 2$. The initial state $|\psi_1(t=0)\rangle = |210\rangle$ evolves as

$$|\psi_1(t)\rangle = \cos(2t)|210\rangle - i \sin(2t)|120\rangle, \quad (15)$$

and the state $|\psi_2(t=0)\rangle = |120\rangle$ evolves as

$$|\psi_2(t)\rangle = -i \sin(2t)|210\rangle + \cos(2t)|120\rangle. \quad (16)$$

Previous results can be straightforwardly generalized to larger systems. Let the length of the system be $L = 3n$ for simplicity. The connected component of the state $|(210)^n$ consists of all possible combinations of patterns 210 and 120. This means that triplets of sites evolve independently, and dynamically the system behaves as a collection of independent two level systems (spins-1/2). From Eq. (15), the initial state $|\psi_n(t=0)\rangle = |(210)^n$ evolves as

$$|\psi_{L=3n}(t)\rangle = \cos^n(2t)|(210)^n + (-i)^n \sin^n(2t)|(120)^n + \dots \quad (17)$$

where “...” denotes contributions of the basis configurations other than $|(210)^n$ or $|(120)^n$. The fidelity is

$$F_{L=3n}(t) = |\langle \psi_n(0) | \psi_n(t) \rangle|^2 = |\cos 2t|^{2n}. \quad (18)$$

It follows that the revivals are perfect, with a period $T_3 = \pi/2$. This result is also valid for the translation-invariant initial state $|(210)^n_T$,

$$|(210)^n_T \equiv \frac{1}{\sqrt{3}} (|(210)^n\rangle + |(021)^n\rangle + |(102)^n\rangle), \quad (19)$$

as the connected subspaces of 210, 021 and 102 do not overlap and therefore evolve independently.

However, an initial state that is both translation symmetric and inversion symmetric has different dynamics. The inverse of the configuration $|(210)^n$ is the configuration $|(012)^n$, which is a translation of the state $|(120)^n$ that belongs to the connected subspace of $|(210)^n$. The initial state

$$|\psi_n^{\text{inv}}(t=0)\rangle = \frac{1}{\sqrt{2}} |(210)^n_T + \frac{1}{\sqrt{2}} |(120)^n_T \quad (20)$$

evolves as

$$|\psi_n^{\text{inv}}(t)\rangle = (\cos^n 2t + (-i)^n \sin^n 2t) |\psi_n^{\text{inv}}(t=0)\rangle + \dots \quad (21)$$

and the fidelity is

$$F_n^{\text{inv}}(t) = |\langle \psi_n^{\text{inv}}(0) | \psi_n^{\text{inv}}(t) \rangle|^2 = |\cos^n 2t + (-i)^n \sin^n 2t|^2. \quad (22)$$

The frequency of the revivals is now doubled, so the period is $T_3^{\text{inv}} = \pi/4$.

B. H_1 model: Cluster approximation

In Sec. II, we have demonstrated that the Hilbert space of H_1 consists of several weakly-connected clusters of configurations. We will now show that this cluster structure is responsible for the H_1 dynamics observed in Fig. 3. Some initial configurations are located in parts of the Hilbert space that are weakly connected to the rest and this leads to the wave-function “getting stuck” in some of those parts instead of spreading through the full Hilbert space. Here we identify such clusters that contain the configurations $(210)^n$, which exhibit interesting dynamics with periodic revivals, as found in Fig. 3.

1. Cluster approximation

As can be observed in Fig. 3, the revival periods are approximately the same for different system sizes. We first focus on the non-trivial case $L = 6$. Fig. 5 shows part of the graph that contains the initial state, $|210210\rangle$. Configurations labelled inside the ellipses denote representatives of an orbit of translation symmetry, i.e., the configurations are translation-invariant such as the one in Eq. (19).

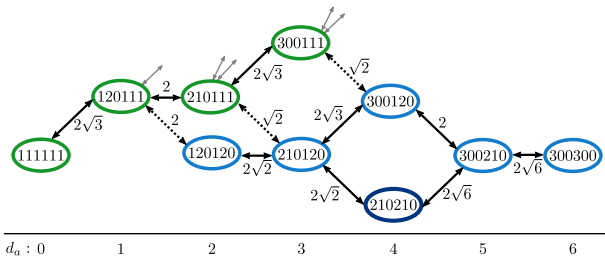


Figure 5. Cluster for H_1 and $L = N_p = 6$. Configurations labelled inside the ellipses are representatives of an orbit of translation symmetry. The minimal cluster is defined by the blue configurations, while green configurations represent the additional components of the extended cluster. Grey arrows connect to configurations outside the extended cluster. The numbers below the graph show the distance d_a from the configuration 111111 evaluated using Eq. (7).

The minimal subcluster of the graph is highlighted in blue color in Fig. 5. This cluster is indeed weakly connected to the rest of the configuration space, as it has only 3 connections that lead outside this cluster (dashed lines) and their hopping coefficients are lower in magnitude than those inside the cluster, meaning that the probability is higher to stay inside the cluster than to leave. Inside this cluster, the evolution of the configuration $|210210\rangle$ can be thought of as two subsystems 210 evolving separately. The evolution of all such configurations at different system sizes can be reduced to the evolution of $L = 3$ subsystems 210, similar to the case of H_3 in the connected subspace of $(210)^n$. The cluster from

Fig. 5 contains all the states given by tensor products of 210, 120 and 300 configurations.

As an example, consider system size $L = 3$. The reduced Hilbert space of the cluster \mathcal{H}^c is spanned by the (non-translation-invariant) configurations

$$\begin{pmatrix} 1 \\ 0 \\ 0 \end{pmatrix} = |300\rangle, \quad \begin{pmatrix} 0 \\ 1 \\ 0 \end{pmatrix} = |210\rangle, \quad \begin{pmatrix} 0 \\ 0 \\ 1 \end{pmatrix} = |120\rangle. \quad (23)$$

The Hamiltonian reduced to this subspace is

$$H_1^{c1} = - \begin{pmatrix} 0 & 2\sqrt{3} & 0 \\ 2\sqrt{3} & 0 & 2 \\ 0 & 2 & 0 \end{pmatrix}, \quad (24)$$

and its eigenvalues are $E_1 = -4$, $E_2 = 4$, $E_3 = 0$. The initial configuration $|210\rangle$ evolves according to

$$\begin{aligned} |\psi_1^{c1}(t)\rangle = & -\frac{i}{2} \sin(4t) \left(\sqrt{3}|300\rangle + |120\rangle \right) \\ & + \cos(4t)|210\rangle. \end{aligned} \quad (25)$$

From this, we can read off the period of revivals: $T_1 = \pi/4$.

Similar to the H_3 case, we can now generalize to larger systems. Within the cluster approximation, triplets of sites again evolve independently, and the dimension of the reduced Hilbert space is

$$\dim \mathcal{H}^c = 3^{L/3}. \quad (26)$$

The time-evolved state within the cluster approximation is given by

$$|\psi_n^c(t)\rangle = \cos^n(4t)|(210)^n\rangle + \dots \quad (27)$$

so the fidelity is

$$F_n^c(t) = |\langle \psi_n^{c1}(0) | \psi_n^{c1}(t) \rangle|^2 = |\cos(4t)|^{2n}. \quad (28)$$

As in the case of H_3 , this result is also valid for the translation-invariant initial state. The period of revivals is $T_1 = \pi/4$, which is the same as for H_3 with a translation and inversion symmetric initial state.

The result of the cluster approximation is compared against the exact result for system size $L = 15$ in Fig. 6. The frequency of the fidelity revival, shown by the blue line in Fig. 6(a), is accurately reproduced in this approximation, however the approximation does not capture the reduction in the magnitude of $F(t)$. Similarly, the dynamics of entanglement entropy, blue line in Fig. 6(b), is only captured at very short times. In particular, we observe that the maximum entanglement within the cluster remains bounded even at long times $t \sim 10$, while the exact entropy continues to increase and takes values that are several times larger.

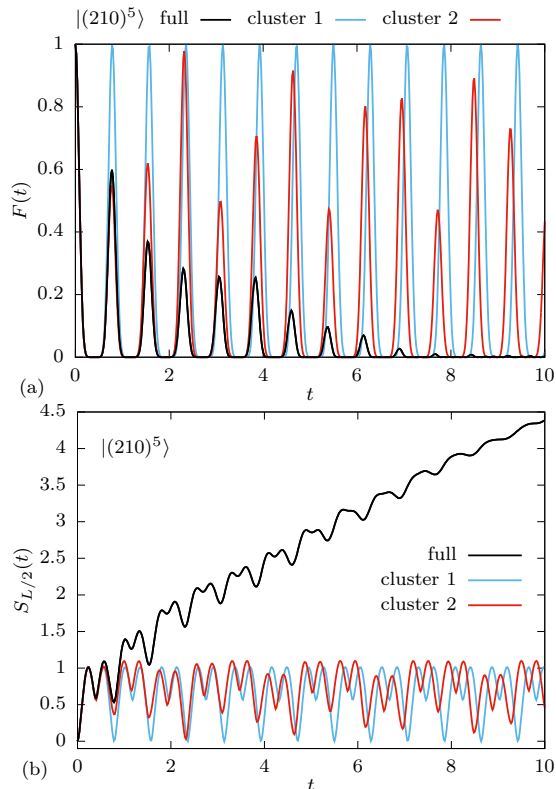


Figure 6. Comparison of the full dynamics against the cluster and extended cluster approximation schemes. We consider the system size $L = 15$ with the initial state $|(210)^5\rangle$. (a) Time evolution of the fidelity. The frequency of revivals is approximately the same in both cases, but the results for the extended cluster show better agreement with the results for the full Hilbert space. (b) Time evolution of the entanglement entropy.

2. Improved cluster approximation

To obtain a more accurate approximation, we now expand the cluster with several neighboring configurations: $|111300\rangle$, $|111210\rangle$, $|111120\rangle$ and $|111111\rangle$. This enlarged cluster contains the minimal cluster studied previously, but it also includes additional configurations shown in green ellipses in Fig. 5. Similar clusters can be defined in larger systems if $L = N_p$ is divisible by 3, by using tensor products of any of the configurations 210, 120, 300 and 111.

The dimension of the extended cluster grows with the system size as

$$\dim \mathcal{H}^{\tilde{c}} = 4^{L/3}, \quad (29)$$

and is thus exponentially larger than the previous cluster approximation. Nevertheless, its dimension is still exponentially smaller compared to the full Hilbert space, and within this approximation it is possible to simulate the dynamics of larger systems, $L \lesssim 30$ – see Fig. 7. The revivals are no longer perfect and their frequency slightly changes with the system size, but it converges for large

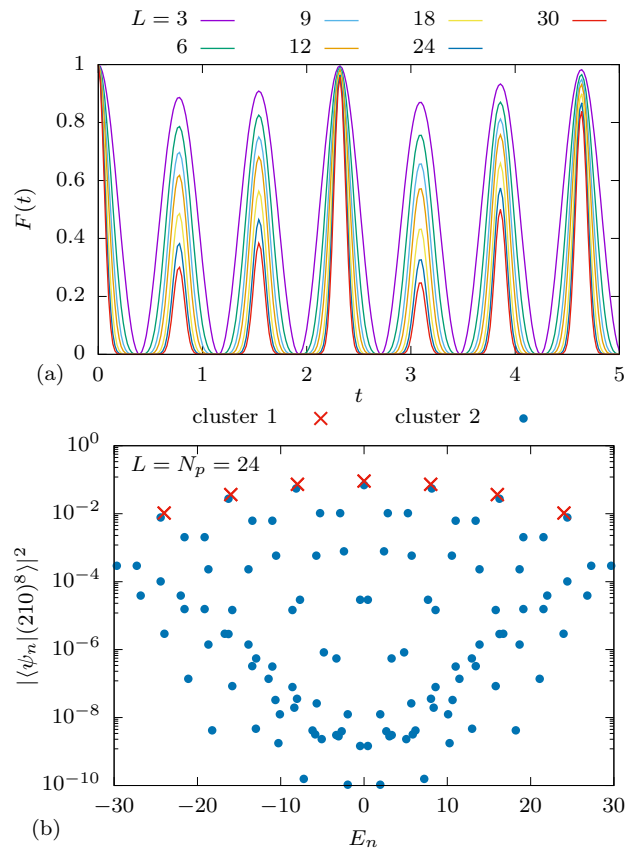


Figure 7. (a) Fidelity $F(t)$, for the Hamiltonian H_1 and initial states $|(210)^n\rangle$, in the extended cluster approximation for various system sizes. (b) Eigenstate overlap with the initial state $|(210)^8\rangle$ plotted on a log scale, for both cluster approximations. In the case of degenerate eigenstates the sum of their overlaps is shown.

L . The frequency is closer to the frequency of revivals for the full Hilbert space than in the original cluster approximation, as previously shown in Fig. 6.

For the initial product state $(210)^n$, it is possible to analytically obtain the fidelity within the improved approximation for arbitrary system size. Similar to the previous methods, it can be shown

$$F_{L=3n}^{\tilde{c}}(t) = 4^n |b^2 \cos(\alpha t) + d^2 \cos(\beta t)|^{2n}, \quad (30)$$

where $\alpha = \sqrt{9 + \sqrt{57}} \approx 4.06815$, $\beta = \sqrt{9 - \sqrt{57}} \approx 1.20423$, $b \approx 0.694113$ and $d \approx 0.134933$. These equations were obtained by solving the eigenproblem for $L = 3$ and generalizing the results to larger systems. The derivation can be found in Appendix D.

Eq. (30) is in excellent agreement with the numerical results from Fig. 7(a). We also found it to be a very good approximation for the translation-invariant initial state when $L \geq 9$ (data not shown). The improved cluster approximation correctly reproduces the short-time dynamics, including the first revival peak, and sets a lower bound for the first peak height – see Figs. 6 and 8.

Fig. 8(a) shows that the negative logarithm of the first

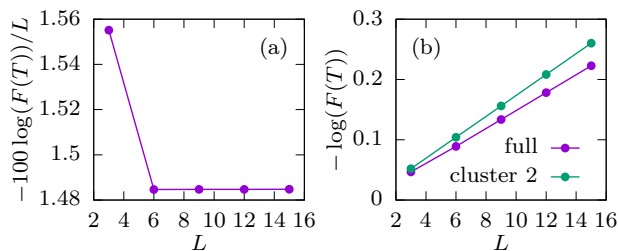


Figure 8. (a) Negative logarithm (base 10) of the first revival peak divided by the system size, $-\log(F(T))/L$, seems to saturate at a finite value in the thermodynamic limit. (b) Comparison of negative logarithm of the first revival peak height for the full dynamics and the improved cluster approximation. The approximation serves as a lower bound.

peak height per site $-\log(F(T))/L$ saturates at a finite value for large L . In Appendix D we show that the first peak height in the improved cluster approximation decreases with the system size as $e^{-0.04L}$. For a completely random state, the fidelity would be $F \sim 1/\dim_{\mathcal{H}}$. In the case $\nu = 1$ and large L , the Hilbert space dimension grows with the system size as

$$\dim_{\mathcal{H}} = \binom{2L-1}{L} \approx \binom{2L}{L} \approx \frac{4^L}{\sqrt{\pi L}}. \quad (31)$$

This results in the fidelity of a random state $F \sim e^{-1.39L}$, which decays significantly faster than the first peak height $e^{-0.04L}$.

The evolution of the entanglement entropy for the extended cluster approximation is shown in Fig. 6(b). Inside the cluster, entropy remains approximately constant with periodic oscillations that have the same frequency as the wave function revivals. Any further growth of the entanglement entropy can be attributed to the spreading of the wave-function outside the cluster.

To illustrate the “leakage” of the wave function outside the cluster, in Fig. 9 we compute the time evolution of the overlap with a cluster, i.e., the probability to remain inside a cluster at time t ,

$$\mathcal{O}_{\text{Cluster}} = \sum_{a \in \text{Cluster}} |\langle a | \psi(t) \rangle|^2. \quad (32)$$

We consider several initial configurations that lie inside or outside the cluster. The configurations initially inside the cluster mostly stay there, and the configuration $|(210)^4\rangle$ that has the highest revivals also has the highest overlap. Similarly, configurations initially outside the cluster continue to have negligible overlaps. The overlap starting from the configuration $|(210)^4\rangle$ approximately predicts the revival peak heights for the full dynamics in Fig. 6.

We conclude this Section by discussing the relation between H_3 and H_1 reduced to the cluster approximation. For the dynamics from the initial state $|(210)^n\rangle$, the two models yield similar results, compare Eqs. (18) and (30). The only difference is that the revival frequency is doubled in the latter case, which can be easily explained by

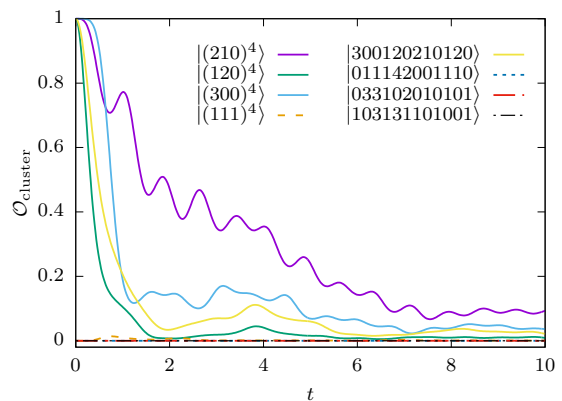


Figure 9. Time evolution of the probability to remain inside the cluster $\mathcal{O}_{\text{Cluster}}$, as defined in Eq. (32), starting from several initial configurations indicated in the legend. Solid lines: configurations initially inside the cluster. Dashed lines: configurations initially outside the cluster (all except $|(111)^4\rangle$ are randomly chosen). Similar results are obtained for the extended cluster (not shown). System size $L = 12$.

the symmetry of the initial state and that of the Hamiltonian. Hamiltonian H_3 is inversion-symmetric. If the initial state is also chosen to be inversion-symmetric, the frequency of the revivals doubles. The period is then $T_3^{\text{inv}} = \pi/4$, which is equal to the period of revivals T_1 of H_1 in the cluster approximation. This is also proved analytically in Sec. IV, see Eq. (22). For comparison, the revival period for the full Hilbert space is approximately 0.77, which is slightly less than $\pi/4 \approx 0.79$. The Hamiltonian H_1 is not inversion-symmetric, so the frequency does not double for an inversion-symmetric initial state, but the revivals are lower in that case. This shows that it is important that the symmetry of the initial state matches the symmetry of the Hamiltonian.

C. Generalization to other clusters

The eigenstates of H_1 , projected to the subspace of the minimal cluster approximation (as defined in Sec. IV B), form several degenerate bands whose eigenenergies are equally spaced in integer multiples of 4. Interestingly, some of these eigenstates approximately survive in the full H_1 model, and they are precisely the eigenstates that have the highest overlap with the configurations $|(210)^n\rangle$. In small system sizes, such as $L = 6$, the surviving eigenstates are also the lowest entropy eigenstates in the middle of the spectrum, which is reminiscent of quantum scars in the PXP model. In larger systems, e.g., $L = 12$, the surviving eigenstates are slightly lower in entropy than their neighbors, but are far from being the lowest entropy eigenstates, as can be seen in Fig. 10. The lowest entropy eigenstates have high overlaps with other configurations, such as $|(3100)^3\rangle$, as shown in Fig. 10(b). In the case of $(210)^n$, the eigenstates surviving in the full system belong to every other band of eigenstates in the

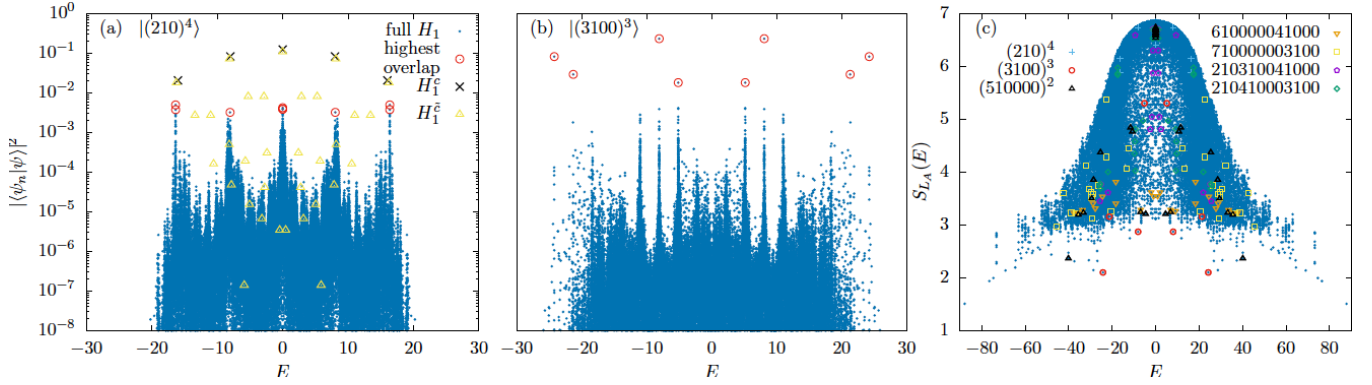


Figure 10. (a) Overlap of the configuration $|(210)^4\rangle$ with all the eigenstates of H_1 , H_1^c and $H_1^{\bar{c}}$ versus the eigenstate energy for sector $k = 0$ and system size $L = N_p = 12$. (b) Same for $|(3100)^3\rangle$. (c) Entanglement entropy, eigenstates which have the highest overlap with some product states are marked in different colors.

cluster approximation and the number of the surviving eigenstates is $n + 1$. For even system sizes this counting includes a zero-energy eigenstate.

Building on the previous observation that some of the low-entropy eigenstates have large weight on $|(3100)^3\rangle$ product state, we have investigated periodic revivals from such a larger class of initial states. We find that robust revivals are associated with initial product states of the form

$$|((N-1)1\underbrace{0\dots 0}_N)^n\rangle, \quad (33)$$

where N is the length of the unit cell ($L = Nn$). For example, some of these configurations are $|(3100)^n\rangle$, $|(41000)^n\rangle$ and $|(510000)^n\rangle$. Combinations of those patterns such as $|310041000\rangle$ also exhibit similar properties, but we will restrict ourselves to the simpler former cases.

We can construct a generalization of the cluster approximation for configurations of the form in Eq. (33). As in the case of $|(210)^n\rangle$, the dynamics inside one unit cell explains the dynamics of the full system. The generalized clusters can be chosen in such a way that their Hilbert spaces are spanned by N configurations

$$|i\rangle = |((N+1-i)(i-1)\underbrace{0\dots 0}_N)^n\rangle, \quad (34)$$

where i takes values $1, 2, \dots, N$. If we consider only one unit cell ($n = 1$), the graph that connects these configurations has a linear structure without any loops, i.e., each configuration $|i\rangle$ is solely connected to the configurations $|i \pm 1\rangle$, except the two configurations at the edges, $|1\rangle$ and $|N\rangle$, which are only connected to $|2\rangle$ and $|N-1\rangle$, respectively.

The projection of the Hamiltonian H_1 to this cluster, which we denote by H_1^c , has a very simple structure: it has the form of a tight-binding chain with the only nonzero matrix elements on the upper and lower diagonals:

$$H_{1;i,i+1}^c = H_{1;i+1,i}^c = (N-i)\sqrt{i(N+1-i)}. \quad (35)$$

The dynamics within a single unit cell under H_1^c corresponds to density fluctuations between the first and the second site. Following the same procedure as previously, we can now diagonalize H_1^c and compute the fidelity time series for the initial configuration $|((N-1)10\dots 0)\rangle$. This result can be directly generalized to configurations of the form $|((N-1)10\dots 0)^n\rangle$. The derivation is valid for both translation-invariant and non-translation-invariant initial configurations, as the cluster in Eq. (34) is disconnected from its translated copies. We stress that this disconnection, namely the absence of a hopping term between $|1(N-1)0\dots 0\rangle$ and $|0N0\dots 0\rangle$, is a consequence of the constraints imposed by H_1 and it would not hold for H_2 . In this way, we have calculated the time evolution of the fidelity starting from the configurations $|(3100)^n\rangle$ (for $n = 1, 2, 3, 4$), $|(41000)^n\rangle$ ($n = 1, 2, 3$) and $|(510000)^n\rangle$ ($n = 1, 2$), and compared it with the exact numerical results for the full H_1 . The cluster approximation captures both the revival frequency and the height of the first peak. Similar to the $|(210)^n\rangle$ case, the approximation can be improved by adding further configurations to the clusters. Moreover, if we want to consider translation-invariant initial states, we can follow the same recipe for $|(210)^n\rangle$ by summing translated patterns with the required phase factors given in terms of momenta in multiples of $2\pi/N$. We have checked that revivals appear in these momentum sectors, with roughly the same frequency.

We note that the configurations with larger units cells thermalize more quickly on shorter timescales, but slower at long times. Initially, the states starting from configurations with smaller N have lower entanglement entropies than those with larger N . The Hilbert spaces of large N unit cells are larger, so the entanglement entropy starting from these configurations rapidly grows to the maximal value for that unit cell. However, the only way for the wave-function to spread through the entire Hilbert space is that a unit cell reaches a state close to $111\dots 111$, so that particles can hop to the other unit cells. This is less likely for large N , and therefore such configurations need

long times to fully thermalize. As a result, smaller N entanglement entropies grow faster and after long enough time they overtake those for larger N . For example, in the case of $L = 12$ and translation-invariant initial states, $(210)^4$ overtakes $(3100)^3$ and $(510000)^2$ around $t \sim 2$, and $(3100)^3$ overtakes $(510000)^2$ around $t \sim 80$.

V. CONCLUSIONS

In this paper, we have introduced three models of bosons with “soft” kinetic constraints, i.e., density-dependent hopping. We have demonstrated that some of these models exhibit similar phenomenology to other realizations of quantum many-body scars, for example the Rydberg atom system.⁵ We have studied quantum dynamics of these systems by performing global quenches from tensor-product initial states. We have shown that both the connectivity of the Hilbert space and the relative magnitude of the hopping coefficients have dramatic effects on the dynamics. For certain initial configurations, the constraints can lead to slow thermalization and revivals in the quantum fidelity. The revival frequency can be predicted by considering an exponentially reduced subset of the Hilbert space. For a family of initial configurations of the form $|(210)^n\rangle$, we have derived analytical expressions for the evolution of quantum fidelity within this approximation, which accurately capture the revival frequency obtained from exact numerical data. Our cluster approximation also explains the structure of some low-entropy eigenstates in the middle of the many-body spectrum. In addition, we have calculated the evolution of two local observables which are experimentally measurable, density correlations between two neighboring sites and density on a single site, and both of them show robust oscillations over a range of system sizes. Finally, we have also shown that the introduced models contain additional special properties, like the exponentially large zero-energy degeneracy which is related to the bipartite structure of the model.

Finally, we comment on the possible experimental realizations of the models we studied. The implementation of a correlated hopping term $(n_k b_i^\dagger b_j)$ in optical lattices has attracted lot of attention due to a possible onset of quantum phases related to high-Tc superconductivity.⁷⁹ An early theoretical proposal exploits asymmetric interactions between the two atomic states in the presence of a state-dependent optical lattice.⁷⁹ As a result, the obtained effective model corresponds to the inversion-symmetric form of H_1 . In addition, the same term has been found to feature as a higher-order correction of the standard Bose-Hubbard model.^{80–83} Although in this case the term typically represents a modification of the regular hopping term of the order of several percent, its contribution was directly measured.^{84,85} More recently, the set of quantum models accessible in cold-atom experiments has been enriched through the technique of Floquet engineering.⁸⁶ As a notable example, a suitable

driving scheme can renormalize or fully suppress the bare tunneling rate.⁸⁷ On top of that, by modulating local interactions an effective model with the density-dependent tunneling term has been engineered.⁸⁸ For the models considered in this paper the most promising is a more recent driving scheme exploiting a double modulation of a local potential and on-site interactions.⁸⁹ Related sophisticated driving schemes have already enabled a realization of dynamical gauge fields^{53,54,90} where both the amplitude and the phase of the effective tunneling are density-dependent.

Note added: During the completion of this work, we became aware of Ref. 91 which identified non-thermal eigenstates and slow dynamics in the quantum East model.

VI. ACKNOWLEDGMENTS

This work was supported by the Ministry of Education, Science, and Technological Development of the Republic of Serbia under Project ON171017. N.R. was supported by the Department of Energy Grant No. [de-sc0016239](#), the National Science Foundation EAGER Grant No. DMR 1643312, Simons Investigator Grant No. 404513, ONR Grant No. N00014-14-1-0330, the Packard Foundation, the Schmidt Fund for Innovative Research, and a Guggenheim Fellowship from the John Simon Guggenheim Memorial Foundation. Z.P. acknowledges support by EPSRC grant EP/R020612/1 and the National Science Foundation under Grant No. NSF PHY-1748958. Statement of compliance with EPSRC policy framework on research data: This publication is theoretical work that does not require supporting research data. Part of the numerical simulations were performed on the PARADOX supercomputing facility at the Scientific Computing Laboratory of the Institute of Physics Belgrade. The authors would also like to acknowledge the contribution of the COST Action CA16221.

Appendix A: Hopping coefficients

Constraints are not the only factor that slows down the dynamics and leads to weakly-entangled eigenstates in spectrum. The relative magnitude of the hopping coefficients between different configurations mapped to each other under the action of the Hamiltonian also has important effects. In order to show this, we introduce two additional Hamiltonians

$$H_{1a} = -J \sum_j \left(b_j^\dagger b_{j+1} n_j^2 + n_{j-1}^2 b_j^\dagger b_{j-1} \right), \quad (A1)$$

$$H_{1b} = -J \sum_j \left(b_j^\dagger b_{j+1} (1 - \delta_{n_j,0}) + (1 - \delta_{n_{j-1},0}) b_j^\dagger b_{j-1} \right). \quad (A2)$$

These two Hamiltonians have the same constraints as the Hamiltonian H_1 and therefore the same graphs as in Fig. 1. However, the particle number operators n_j are squared in H_{1a} and replaced with delta functions ($1 - \delta_{n_j,0}$) in H_{1b} . This makes the clusters from Section IV B even less connected to the rest of the configurations in the case of H_{1a} and more connected in the case of H_{1b} .

As anticipated, the revivals become more prominent for H_{1a} , with fidelity peaks reaching more than 95%, while the peaks almost disappear for H_{1b} , as illustrated in Fig. 11(a). In addition, the entanglement entropy quickly saturates in the case H_{1b} , while the growth is significantly suppressed in the case of H_{1a} , as can be observed in Fig. 11(b). The distribution of entanglement entropy across all eigenstates is also affected by the change of coefficients (not shown). H_{1a} has a spectrum with many low-entropy eigenstates, while the spectrum of H_{1b} is almost thermal and resembles that of H_2 . The probability distribution of consecutive gaps in the energy spectrum of H_{1a} is close to the Poisson distribution, which implies that H_{1a} is almost integrable. On the other hand, the distribution for H_{1a} is Wigner-Dyson, like in H_1 .

Appendix B: Bipartite structure of H_1

We have shown in Sec. IIB that the H_1 model is bipartite for open boundary conditions irrespective of the system size L parity or for periodic boundary conditions when L is even. We prove in this appendix that this property of H_1 holds true when L is odd and $\nu = 1$.

Due to the constraints imposed by H_1 , a particle cannot hop to an empty site to its left. At the filling factor $\nu = 1$, all configurations except 111...111 contain at least one empty site. These configurations can be connected to 111...111 by hoppings only to the right, which is also the shortest possible path d_a , defined in Eq. (7). The empty sites can be filled only with particles that come from the site on their left, as hopping from the other side is forbidden. This implies that at least for one pair of adjacent sites (an empty site and the filled one on its right) there will be no particles hopping between them on the path to 111...111. We can then redefine the numbering of sites to start from the filled site in this pair. This is equivalent to setting the right (filled) site as the first and the left (empty) site as the last site in the chain and imposing open boundary conditions. In this way, no two odd sites will be coupled and the argument that the absolute difference between the numbers of particles on even and odd sites can only change by ± 1 will still be valid.

Unlike H_1 , H_2 in the same geometry is not bipartite. The reason for this is that there are no constraints in the case of H_2 , so the shortest path to 111...111 can include hoppings both to the right and to the left, which means that it is not always possible to choose the numbering in such a way that no two odd sites are coupled. Because

of the open boundary conditions, the Hamiltonian H_3 in its largest connected component is also bipartite for all system sizes.

Appendix C: Zero modes

An interesting feature of H_1 model is the large number of zero energy states in the middle of its spectrum. The number of these zero modes, found by brute force diagonalization, is listed in Table I for different system sizes and momentum sectors. Similar property is found for H_2 – see Table II, with the notable difference that there are no zero modes when the number of sites L is odd.

$L = N_p$	$\frac{kL}{2\pi}$										total	
	0	1	2	3	4	5	6	7	8	9		10
2	0	1										1
3	0	1	1									2
4	2	0	1	0								3
5	2	1	1	1	1							6
6	2	3	0	4	0	3						12
7	2	3	3	3	3	3	3					20
8	10	0	8	0	9	0	8	0				35
9	8	8	8	7	8	8	7	8	8			70
10	4	25	2	25	2	26	2	25	2	25		138
11	22	23	23	23	23	23	23	23	23	23	23	252

Table I. The number of zero-energy states for the Hamiltonian H_1 and different system sizes. The number of states is resolved per momentum sectors, denoted by their momentum indices i that parametrize the momenta $k_i = \frac{2\pi}{L}i$.

$L = N_p$	$\frac{kL}{2\pi}$										total	
	0	1	2	3	4	5	6	7	8	9		10
2	0	1										1
3	0	0	0									0
4	2	0	1	0								3
5	0	0	0	0	0							0
6	0	3	0	4	0	3						10
7	0	0	0	0	0	0	0					0
8	10	0	8	0	9	0	8	0				35
9	0	0	0	0	0	0	0	0	0			0
10	0	25	0	26	0	26	0	26	0	25		128
11	0	0	0	0	0	0	0	0	0	0	0	0

Table II. Same as Table I for the Hamiltonian H_2 .

The origin of the zero modes is the underlying bipartite structure of the Hamiltonian.^{73,74} As explained in Section IIB, all the basis configurations of the H_1 model can be separated into two disjoint classes, and the action of the Hamiltonian H_1 only connects configurations in one class to the configurations in the other class, while

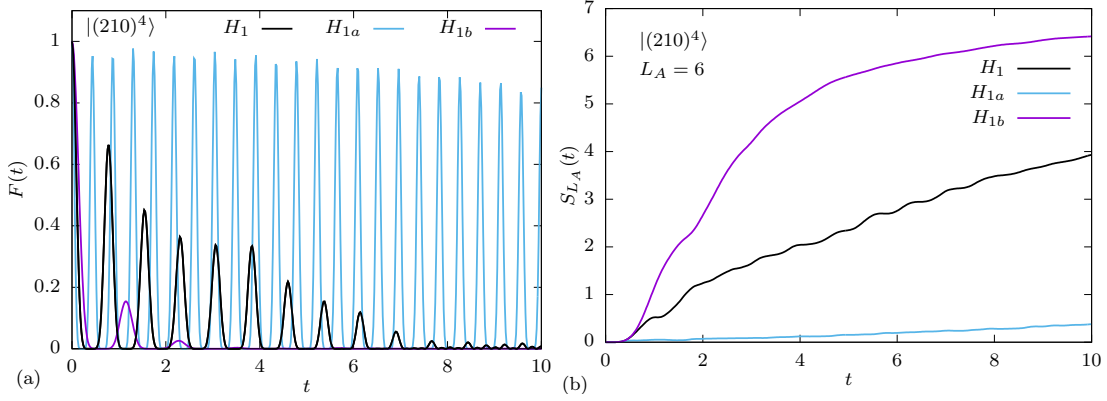


Figure 11. Time evolution of (a) fidelity $|\langle \psi(t) | \psi(0) \rangle|^2$ and (b) entanglement entropy $S_{L_A=6}(t)$ governed by three different Hamiltonians, H_1 , H_{1a} and H_{1b} . System size $L = 12$ and initial state $|(210)^4\rangle$.

H_1 does not connect configurations within the same class. For example, a graph that shows how the configurations for $L = N_p = 4$ are connected is displayed in Fig. 12. Here we will refer to the two classes as the “green” (even) and the “red” (odd) configurations. Each basis configuration can be uniquely assigned a green or a red label according to the parity of its distance d_a , Eq. (7), from the configuration $|111\dots 111\rangle$. If this number is even, the configuration is green, and if it is odd, the configuration is red.

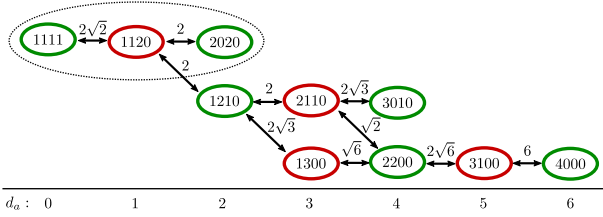


Figure 12. Bipartite graph for H_1 and $L = N_p = 4$. The two classes of configurations are shown in green (even) and red (odd) ellipses. The configurations are written in the translation-invariant basis. The arrows represent the action of the Hamiltonian H_1 and the numbers above the arrows are the magnitudes of the corresponding hopping coefficients. The numbers below the graph show the distance d_a from the configuration 1111 .

This separation into two classes is a consequence of the constraints present in the Hamiltonian H_1 . Hamiltonians without such constraints, for example H_2 or the standard Bose-Hubbard model, do not exhibit this bipartite structure for odd system sizes, see Section II B and Appendix B more details. In these cases, it is not possible to uniquely determine whether a particular configuration is green or red. The lack of bipartite structure is the reason for the absence of zero energy eigenstates of H_2 in odd dimensions, which was observed in Table II. However, the configuration space of H_2 is still bipartite in even dimensions, allowing for the existence of some zero modes in those cases.

Low-entropy zero-energy states can be constructed as superpositions of either only green or only red configurations. For example, in the case of $L = N_p = 4$, the simplest and therefore the lowest-entropy zero mode can be constructed using only two green product states (encircled by a dashed line in Fig. 12)

$$|\psi_0\rangle = \frac{1}{\sqrt{3}}|1111\rangle - \sqrt{\frac{2}{3}}|2020\rangle_T, \quad (\text{C1})$$

where $|\dots\rangle_T$ was defined in Eq. (19). There is another zero mode in this case, and it can be formed by adding more green configurations to the superposition. The number of zero-energy eigenstates is related to the difference between the numbers of green and red configurations,⁷³ as we will now explain.

As the Hamiltonian H_1 only connects green configurations to red configurations and red to green, we can rewrite it in the following way:

$$H_1 = \sum_{i,j} c_{ij} |R_i\rangle \langle G_j| + \sum_{i,j} c_{ij}^\dagger |G_j\rangle \langle R_i|, \quad (\text{C2})$$

where $|R_i\rangle$ are the red product states and $|G_j\rangle$ are green. Its square, H_1^2 , connects green configurations to green and red to red, and it is therefore block diagonal. The blocks are CC^\dagger and $C^\dagger C$, where C is a matrix with the elements c_{ij} . The dimensions of C are $r \times g$, where r is the number of red configurations and g of green. C and C^\dagger can be factorized using singular value decomposition. From this structure we can see that the energy spectrum is symmetric around zero and that the minimal number of zero-energy states is $|g - r|$. The zero-energy eigenvectors can also be obtained as the ground states of H_1^2 . Similar analysis and counting of the zero modes in PXP model was performed in Ref. 6 and 92.

Table III shows the difference between the numbers of red and green states $g - r$ for different system sizes and the number of zero-energy states N_0 in those systems. The number of zero-energy states, found by exact diagonalization, in all cases satisfies the anticipated inequality

$N_0 \geq |g - r|$. In fact, the bound is almost always saturated, $N_0 = |g - r|$, except when $L = N_p = 4n + 2$, $n \in \mathbb{Z}$. Interestingly, the minimal number of zero modes $|g - r|$ for $L = N_p = 4n$ is equal to the Hilbert space dimension for $L = N_p = 2n$ (both total and for $k = 0$ sector only). This leads to the conclusion that the number of zero-energy states grows exponentially with the system size. It can also be noticed that the total difference $g - r$ for $L = N_p = 2n + 1$ is always twice the difference for $L = N_p = 2n$.

$L = N_p$	all sectors		$k = 0$	
	$g - r$	N_0	$g - r$	N_0
2	-1	1	0	0
3	-2	2	0	0
4	3	3	2	2
5	6	6	2	2
6	-10	12	0	2
7	-20	20	-2	2
8	35	35	10	10
9	70	70	8	8
10	-126	138	0	4
11	-252	252	-22	22
12	462	NA	80	80
13	924	NA	72	NA
14	-1716	NA	0	NA
15	-3432	NA	-228	NA
16	6435	NA	810	NA

Table III. The difference between the number of green and red configurations $g - r$ and the number of zero-energy states N_0 (determined by exact diagonalization) for different system sizes. Overall, the derived bound for the number of zero modes is found to be very tight in finite systems where it can be independently confirmed by explicit diagonalization (“NA” denotes cases where this was not possible).

Appendix D: Derivation of fidelity in the extended cluster approximation for $|(210)^n\rangle$

For system size $L = 3$, the Hilbert space of the extended cluster is spanned by only four configurations:

$$\begin{pmatrix} 1 \\ 0 \\ 0 \\ 0 \end{pmatrix} = |300\rangle, \quad \begin{pmatrix} 0 \\ 1 \\ 0 \\ 0 \end{pmatrix} = |210\rangle, \quad \begin{pmatrix} 0 \\ 0 \\ 1 \\ 0 \end{pmatrix} = |120\rangle, \quad \begin{pmatrix} 0 \\ 0 \\ 0 \\ 1 \end{pmatrix} = |111\rangle, \quad (D1)$$

The Hamiltonian reduced to this subspace is

$$H_1^{\tilde{c}} = - \begin{pmatrix} 0 & 2\sqrt{3} & 0 & 0 \\ 2\sqrt{3} & 0 & 2 & 0 \\ 0 & 2 & 0 & \sqrt{2} \\ 0 & 0 & \sqrt{2} & 0 \end{pmatrix}. \quad (D2)$$

Its eigenvalues are

$$E_1 = -\alpha, \quad E_2 = \alpha, \quad E_3 = -\beta, \quad E_4 = \beta, \quad (D3)$$

and its eigenvectors

$$|1\rangle = \begin{pmatrix} a \\ b \\ c \\ d \end{pmatrix}, \quad |2\rangle = \begin{pmatrix} -a \\ b \\ -c \\ d \end{pmatrix}, \quad |3\rangle = \begin{pmatrix} -c \\ -d \\ a \\ b \end{pmatrix}, \quad |4\rangle = \begin{pmatrix} c \\ -d \\ -a \\ b \end{pmatrix}, \quad (D4)$$

where $\alpha = \sqrt{9 + \sqrt{57}} \approx 4.06815$, $\beta = \sqrt{9 - \sqrt{57}} \approx 1.20423$, $a \approx 0.591050$, $b \approx 0.694113$, $c \approx 0.388150$ and $d \approx 0.134933$. There are no simple analytical expressions for the coefficients a , b , c and d .

The configuration $|210\rangle$ evolves as

$$\begin{aligned} |\psi_1^{\tilde{c}}(t)\rangle &= -2i(ab \sin \alpha t + cd \sin \beta t) |300\rangle \\ &\quad + 2(b^2 \cos \alpha t + d^2 \cos \beta t) |210\rangle \\ &\quad - 2i(bc \sin \alpha t - ad \sin \beta t) |120\rangle \\ &\quad + 2bd(\cos \alpha t - \cos \beta t) |111\rangle, \end{aligned} \quad (D5)$$

which can also be generalized to larger systems

$$|\Psi_n^{\tilde{c}}(t)\rangle = |(210)^n(t)\rangle = 2^n (b^2 \cos \alpha t + d^2 \cos \beta t)^n |(210)^n\rangle + \dots \quad (D6)$$

Finally, the fidelity evolves as

$$\begin{aligned} F_n^{\tilde{c}}(t) &= |\langle \Psi_n^{\tilde{c}}(0) | \Psi_n^{\tilde{c}}(t) \rangle|^2 \\ &= 4^n |b^2 \cos \alpha t + d^2 \cos \beta t|^{2n}. \end{aligned} \quad (D7)$$

The period of revivals is approximately $T \approx \pi/\alpha \approx 0.772241$, and the first peak height exponentially decreases as

$$\begin{aligned} F_{L=3n}^{\tilde{c}}(T) &= 4^n |d^2 \cos \frac{\pi\beta}{\alpha} - b^2|^{2n} \approx 0.887017^n \\ &\approx e^{-0.119891n} \approx e^{-0.039964L}. \end{aligned} \quad (D8)$$

Eqs. (D6) and (30) are exact for non-translation-invariant initial states, but just an approximation for the translation symmetric case. This is due to the fact that different translations of 300, 210 and 120 no longer evolve independently in that case, as they are connected to each other through the configuration 111. However, this approximation becomes better with increasing the system size, as the configuration $(111)^n$ becomes further away from the initial state $(210)^n$ and the probability that this configuration will be reached decreases.

- ¹ Eric J. Heller, “Bound-state eigenfunctions of classically chaotic hamiltonian systems: Scars of periodic orbits,” *Phys. Rev. Lett.* **53**, 1515 (1984).
- ² S. Sridhar, “Experimental observation of scarred eigenfunctions of chaotic microwave cavities,” *Phys. Rev. Lett.* **67**, 785 (1991).
- ³ C. M. Marcus, A. J. Rimbberg, R. M. Westervelt, P. F. Hopkins, and A. C. Gossard, “Conductance fluctuations and chaotic scattering in ballistic microstructures,” *Phys. Rev. Lett.* **69**, 506 (1992).
- ⁴ P. B. Wilkinson, T. M. Fromhold, L. Eaves, F. W. Sheard, N. Miura, and T. Takamasu, “Observation of scarred wavefunctions in a quantum well with chaotic electron dynamics,” *Nature* **380**, 608 (1996).
- ⁵ Hannes Bernien, Sylvain Schwartz, Alexander Keesling, Harry Levine, Ahmed Omran, Hannes Pichler, Soonwon Choi, Alexander S. Zibrov, Manuel Endres, Markus Greiner, Vladan Vuletic, and Mikhail D. Lukin, “Probing many-body dynamics on a 51-atom quantum simulator,” *Nature* **551**, 579 (2017).
- ⁶ C. J. Turner, A. A. Michailidis, D. A. Abanin, M. Serbyn, and Z. Papić, “Weak ergodicity breaking from quantum many-body scars,” *Nat. Phys.* **14**, 745 (2018).
- ⁷ Wen Wei Ho, Soonwon Choi, Hannes Pichler, and Mikhail D. Lukin, “Periodic orbits, entanglement, and quantum many-body scars in constrained models: Matrix product state approach,” *Phys. Rev. Lett.* **122**, 040603 (2019).
- ⁸ Peter Schauf, Marc Cheneau, Manuel Endres, Takeshi Fukuhara, Sebastian Hild, Ahmed Omran, Thomas Pohl, Christian Gross, Stefan Kuhr, and Immanuel Bloch, “Observation of spatially ordered structures in a two-dimensional Rydberg gas,” *Nature* **491**, 87 (2012).
- ⁹ Henning Labuhn, Daniel Barredo, Sylvain Ravets, Sylvain de Léséleuc, Tommaso Macrì, Thierry Lahaye, and Antoine Browaeys, “Tunable two-dimensional arrays of single Rydberg atoms for realizing quantum Ising models,” *Nature* **534**, 667 (2016).
- ¹⁰ Pasquale Calabrese and John Cardy, “Time dependence of correlation functions following a quantum quench,” *Phys. Rev. Lett.* **96**, 136801 (2006).
- ¹¹ Toshiya Kinoshita, Trevor Wenger, and David S. Weiss, “A quantum Newton’s cradle,” *Nature* **440**, 900 (2006).
- ¹² Michael Schreiber, Sean S. Hodgman, Pranjal Bordia, Henrik P. Lüschen, Mark H. Fischer, Ronen Vosk, Ehud Altman, Ulrich Schneider, and Immanuel Bloch, “Observation of many-body localization of interacting fermions in a quasirandom optical lattice,” *Science* **349**, 842 (2015).
- ¹³ J. Smith, A. Lee, P. Richerme, B. Neyenhuis, P. W. Hess, P. Hauke, M. Heyl, D. A. Huse, and C. Monroe, “Many-body localization in a quantum simulator with programmable random disorder,” *Nat. Phys.* **12**, 907 (2016).
- ¹⁴ G. Kucsko, S. Choi, J. Choi, P. C. Maurer, H. Zhou, R. Landig, H. Sumiya, S. Onoda, J. Isoya, F. Jelezko, E. Demler, N. Y. Yao, and M. D. Lukin, “Critical thermalization of a disordered dipolar spin system in diamond,” *Phys. Rev. Lett.* **121**, 023601 (2018).
- ¹⁵ Adam M. Kaufman, M. Eric Tai, Alexander Lukin, Matthew Rispoli, Robert Schittko, Philipp M. Preiss, and Markus Greiner, “Quantum thermalization through entanglement in an isolated many-body system,” *Science* **353**, 794 (2016).
- ¹⁶ Soonwon Choi, Christopher J. Turner, Hannes Pichler, Wen Wei Ho, Alexios A. Michailidis, Zlatko Papić, Maksym Serbyn, Mikhail D. Lukin, and Dmitry A. Abanin, “Emergent SU(2) dynamics and perfect quantum many-body scars,” *Phys. Rev. Lett.* **122**, 220603 (2019).
- ¹⁷ J. M. Deutsch, “Quantum statistical mechanics in a closed system,” *Phys. Rev. A* **43**, 2046 (1991).
- ¹⁸ Mark Srednicki, “Chaos and quantum thermalization,” *Phys. Rev. E* **50**, 888 (1994).
- ¹⁹ C. J. Turner, A. A. Michailidis, D. A. Abanin, M. Serbyn, and Z. Papić, “Quantum scarred eigenstates in a Rydberg atom chain: Entanglement, breakdown of thermalization, and stability to perturbations,” *Phys. Rev. B* **98**, 155134 (2018).
- ²⁰ Thomas Iadecola, Michael Schecter, and Shenglong Xu, “Quantum Many-Body Scars and Space-Time Crystalline Order from Magnon Condensation,” arXiv e-prints (2019), arXiv:1903.10517 [cond-mat.str-el].
- ²¹ Sanjay Moudgalya, Stephan Rachel, B. Andrei Bernevig, and Nicolas Regnault, “Exact excited states of nonintegrable models,” *Phys. Rev. B* **98**, 235155 (2018).
- ²² Sanjay Moudgalya, Nicolas Regnault, and B. Andrei Bernevig, “Entanglement of exact excited states of Affleck-Kennedy-Lieb-Tasaki models: Exact results, many-body scars, and violation of the strong eigenstate thermalization hypothesis,” *Phys. Rev. B* **98**, 235156 (2018).
- ²³ Cheng-Ju Lin and Olexei I. Motrunich, “Exact quantum many-body scar states in the Rydberg-blockaded atom chain,” *Phys. Rev. Lett.* **122**, 173401 (2019).
- ²⁴ Vedika Khemani, Chris R. Laumann, and Anushya Chandran, “Signatures of integrability in the dynamics of Rydberg-blockaded chains,” *Phys. Rev. B* **99**, 161101 (2019).
- ²⁵ A. A. Michailidis, C. J. Turner, Z. Papić, D. A. Abanin, and M. Serbyn, “Slow quantum thermalization and many-body revivals from mixed phase space,” arXiv e-prints (2019), arXiv:1905.08564 [quant-ph].
- ²⁶ Marton Kormos, Mario Collura, Gabor Takács, and Pasquale Calabrese, “Real-time confinement following a quantum quench to a non-integrable model,” *Nat. Phys.* **13**, 246 (2016).
- ²⁷ Andrew J. A. James, Robert M. Konik, and Neil J. Robinson, “Nonthermal states arising from confinement in one and two dimensions,” *Phys. Rev. Lett.* **122**, 130603 (2019).
- ²⁸ Neil J. Robinson, Andrew J. A. James, and Robert M. Konik, “Signatures of rare states and thermalization in a theory with confinement,” *Phys. Rev. B* **99**, 195108 (2019).
- ²⁹ Oskar Vafek, Nicolas Regnault, and B. Andrei Bernevig, “Entanglement of Exact Excited Eigenstates of the Hubbard Model in Arbitrary Dimension,” *SciPost Phys.* **3**, 043 (2017).
- ³⁰ Thomas Iadecola and Marko Žnidarič, “Exact localized and ballistic eigenstates in disordered chaotic spin ladders and the Fermi-Hubbard model,” *Phys. Rev. Lett.* **123**, 036403 (2019).
- ³¹ Asmi Haldar, Diptiman Sen, Roderich Moessner, and Arnab Das, “Scars in strongly driven Floquet matter: resonance vs emergent conservation laws,” arXiv e-prints (2019), arXiv:1909.04064 [cond-mat.other].
- ³² Sanjay Moudgalya, B. Andrei Bernevig, and Nicolas Reg-

- nault, “Quantum Many-body Scars in a Landau Level on a Thin Torus,” arXiv e-prints (2019), [arXiv:1906.05292 \[cond-mat.str-el\]](#).
- ³³ Shriya Pai and Michael Pretko, “Dynamical scar states in driven fracton systems,” *Phys. Rev. Lett.* **123**, 136401 (2019).
- ³⁴ Vedika Khemani and Rahul Nandkishore, “Local constraints can globally shatter Hilbert space: a new route to quantum information protection,” arXiv e-prints (2019), [arXiv:1904.04815 \[cond-mat.stat-mech\]](#).
- ³⁵ Pablo Sala, Tibor Rakovszky, Ruben Verresen, Michael Knap, and Frank Pollmann, “Ergodicity-breaking arising from Hilbert space fragmentation in dipole-conserving Hamiltonians,” arXiv e-prints (2019), [arXiv:1904.04266 \[cond-mat.str-el\]](#).
- ³⁶ Vedika Khemani, Michael Hermele, and Rahul M. Nandkishore, “Localization from shattering: higher dimensions and physical realizations,” arXiv e-prints (2019), [arXiv:1910.01137 \[cond-mat.stat-mech\]](#).
- ³⁷ Naoto Shiraishi and Takashi Mori, “Systematic construction of counterexamples to the eigenstate thermalization hypothesis,” *Phys. Rev. Lett.* **119**, 030601 (2017).
- ³⁸ Luca D’Alessio, Yariv Kafri, Anatoli Polkovnikov, and Marcos Rigol, “From quantum chaos and eigenstate thermalization to statistical mechanics and thermodynamics,” *Adv. Phys.* **65**, 239 (2016).
- ³⁹ Christian Gogolin and Jens Eisert, “Equilibration, thermalisation, and the emergence of statistical mechanics in closed quantum systems,” *Rep. Prog. Phys.* **79**, 056001 (2016).
- ⁴⁰ Seulgi Ok, Kenny Choo, Christopher Mudry, Claudio Castelnovo, Claudio Chamon, and Titus Neupert, “Topological many-body scar states in dimensions 1, 2, and 3,” arXiv e-prints (2019), [arXiv:1901.01260 \[cond-mat.other\]](#).
- ⁴¹ Kieran Bull, Ivar Martin, and Z. Papić, “Systematic construction of scarred many-body dynamics in 1D lattice models,” *Phys. Rev. Lett.* **123**, 030601 (2019).
- ⁴² Igor Lesanovsky and Hosho Katsura, “Interacting Fibonacci anyons in a Rydberg gas,” *Phys. Rev. A* **86**, 041601 (2012).
- ⁴³ Adrian Feiguin, Simon Trebst, Andreas W. W. Ludwig, Matthias Troyer, Alexei Kitaev, Zhenghan Wang, and Michael H. Freedman, “Interacting anyons in topological quantum liquids: The golden chain,” *Phys. Rev. Lett.* **98**, 160409 (2007).
- ⁴⁴ Simon Trebst, Eddy Ardonne, Adrian Feiguin, David A. Huse, Andreas W. W. Ludwig, and Matthias Troyer, “Collective states of interacting Fibonacci anyons,” *Phys. Rev. Lett.* **101**, 050401 (2008).
- ⁴⁵ Anushya Chandran, Fiona J. Burnell, and Shivaji L. Sondhi, “Do Rydberg chains yield Fibonacci anyons?” arXiv e-prints (2019), [arXiv:1909.09652 \[quant-ph\]](#).
- ⁴⁶ A. Chandran, Marc D. Schulz, and F. J. Burnell, “The eigenstate thermalization hypothesis in constrained Hilbert spaces: A case study in non-Abelian anyon chains,” *Phys. Rev. B* **94**, 235122 (2016).
- ⁴⁷ Zhihao Lan and Stephen Powell, “Eigenstate thermalization hypothesis in quantum dimer models,” *Phys. Rev. B* **96**, 115140 (2017).
- ⁴⁸ Zhihao Lan, Merlijn van Horssen, Stephen Powell, and Juan P. Garrahan, “Quantum slow relaxation and metastability due to dynamical constraints,” *Phys. Rev. Lett.* **121**, 040603 (2018).
- ⁴⁹ A. Smith, J. Knolle, R. Moessner, and D. L. Kovrizhin, “Absence of ergodicity without quenched disorder: From quantum disentangled liquids to many-body localization,” *Phys. Rev. Lett.* **119**, 176601 (2017).
- ⁵⁰ Marlon Brenes, Marcello Dalmonte, Markus Heyl, and Antonello Scardicchio, “Many-body localization dynamics from gauge invariance,” *Phys. Rev. Lett.* **120**, 030601 (2018).
- ⁵¹ Federica M. Surace, Paolo P. Mazza, Giuliano Giudici, Alessio Lerose, Andrea Gambassi, and Marcello Dalmonte, “Lattice gauge theories and string dynamics in Rydberg atom quantum simulators,” arXiv e-prints (2019), [arXiv:1902.09551 \[cond-mat.quant-gas\]](#).
- ⁵² Giuseppe Magnifico, Marcello Dalmonte, Paolo Facchi, Saverio Pascazio, Francesco V. Pepe, and Elisa Ercolessi, “Real Time Dynamics and Confinement in the \mathbb{Z}_n Schwinger-Weyl lattice model for 1+1 QED,” arXiv e-prints (2019), [arXiv:1909.04821 \[quant-ph\]](#).
- ⁵³ Frederik Görg, Kilian Sandholzer, Joaquín Minguzzi, Rémi Desbuquois, Michael Messer, and Tilman Esslinger, “Realisation of density-dependent peierls phases to couple dynamical gauge fields to matter,” *Nat. Phys.* (2019), [10.1038/s41567-019-0615-4](#).
- ⁵⁴ Christian Schweizer, Fabian Grusdt, Moritz Berngruber, Luca Barbiero, Eugene Demler, Nathan Goldman, Immanuel Bloch, and Monika Aidelsburger, “Floquet approach to \mathbb{Z}_2 lattice gauge theories with ultracold atoms in optical lattices,” arXiv e-prints (2019), [arXiv:1901.07103 \[cond-mat.quant-gas\]](#).
- ⁵⁵ Dmitry A. Abanin, Ehud Altman, Immanuel Bloch, and Maksym Serbyn, “Colloquium: Many-body localization, thermalization, and entanglement,” *Rev. Mod. Phys.* **91**, 021001 (2019).
- ⁵⁶ K. Binder and A. P. Young, “Spin glasses: Experimental facts, theoretical concepts, and open questions,” *Rev. Mod. Phys.* **58**, 801 (1986).
- ⁵⁷ Ludovic Berthier and Giulio Biroli, “Theoretical perspective on the glass transition and amorphous materials,” *Rev. Mod. Phys.* **83**, 587 (2011).
- ⁵⁸ Giulio Biroli and Juan P. Garrahan, “Perspective: The glass transition,” *J. Chem. Phys.* **138**, 12A301 (2013).
- ⁵⁹ Glenn H. Fredrickson and Hans C. Andersen, “Kinetic Ising model of the glass transition,” *Phys. Rev. Lett.* **53**, 1244 (1984).
- ⁶⁰ R. G. Palmer, D. L. Stein, E. Abrahams, and P. W. Anderson, “Models of hierarchically constrained dynamics for glassy relaxation,” *Phys. Rev. Lett.* **53**, 958 (1984).
- ⁶¹ Giuseppe Carleo, Federico Becca, Marco Schiró, and Michele Fabrizio, “Localization and glassy dynamics of many-body quantum systems,” *Sci. Rep.* **2**, 243 (2012).
- ⁶² Wojciech De Roeck and François Huveneers, “Asymptotic quantum many-body localization from thermal disorder,” *Commun. Math. Phys.* **332**, 1017 (2014).
- ⁶³ M. Schiulaz and M. Müller, “Ideal quantum glass transitions: Many-body localization without quenched disorder,” in *American Institute of Physics Conference Series*, American Institute of Physics Conference Series, Vol. 1610 (2014) pp. 11–23, [arXiv:1309.1082](#).
- ⁶⁴ N. Y. Yao, C. R. Laumann, J. I. Cirac, M. D. Lukin, and J. E. Moore, “Quasi-many-body localization in translation-invariant systems,” *Phys. Rev. Lett.* **117**, 240601 (2016).
- ⁶⁵ Z. Papić, E. Miles Stoudenmire, and Dmitry A. Abanin, “Many-body localization in disorder-free systems: The importance of finite-size constraints,” *Ann. Phys.* **362**, 714 (2015).

- ⁶⁶ Merlijn van Horssen, Emanuele Levi, and Juan P. Garrahan, “Dynamics of many-body localization in a translation-invariant quantum glass model,” *Phys. Rev. B* **92**, 100305 (2015).
- ⁶⁷ Thomas Veness, Fabian H. L. Essler, and Matthew P. A. Fisher, “Quantum disentangled liquid in the half-filled Hubbard model,” *Phys. Rev. B* **96**, 195153 (2017).
- ⁶⁸ A. Smith, J. Knolle, D. L. Kovrizhin, and R. Moessner, “Disorder-free localization,” *Phys. Rev. Lett.* **118**, 266601 (2017).
- ⁶⁹ Isaac H. Kim and Jeongwan Haah, “Localization from superselection rules in translationally invariant systems,” *Phys. Rev. Lett.* **116**, 027202 (2016).
- ⁷⁰ H. Yarloo, A. Langari, and A. Vaezi, “Anyonic self-induced disorder in a stabilizer code: Quasi many-body localization in a translational invariant model,” *Phys. Rev. B* **97**, 054304 (2018).
- ⁷¹ Alexios A. Michailidis, Marko Žnidarič, Mariya Medvedyeva, Dmitry A. Abanin, Tomaž Prosen, and Z. Papić, “Slow dynamics in translation-invariant quantum lattice models,” *Phys. Rev. B* **97**, 104307 (2018).
- ⁷² Merlijn van Horssen, Emanuele Levi, and Juan P. Garrahan, “Dynamics of many-body localization in a translation-invariant quantum glass model,” *Phys. Rev. B* **92**, 100305 (2015).
- ⁷³ Bill Sutherland, “Localization of electronic wave functions due to local topology,” *Phys. Rev. B* **34**, 5208 (1986).
- ⁷⁴ M. Inui, S. A. Trugman, and Elihu Abrahams, “Unusual properties of midband states in systems with off-diagonal disorder,” *Phys. Rev. B* **49**, 3190 (1994).
- ⁷⁵ Vadim Oganesyan and David A. Huse, “Localization of interacting fermions at high temperature,” *Phys. Rev. B* **75**, 155111 (2007).
- ⁷⁶ Luca D’Alessio and Marcos Rigol, “Long-time behavior of isolated periodically driven interacting lattice systems,” *Phys. Rev. X* **4**, 041048 (2014).
- ⁷⁷ Madan Lal Mehta, *Random matrices*, Vol. 142 (Elsevier, 2004).
- ⁷⁸ Vincenzo Alba, Maurizio Fagotti, and Pasquale Calabrese, “Entanglement entropy of excited states,” *J. Stat. Mech.* **2009**, P10020 (2009).
- ⁷⁹ Maria Eckholt and Juan José García-Ripoll, “Correlated hopping of bosonic atoms induced by optical lattices,” *New J. Phys.* **11**, 093028 (2009).
- ⁸⁰ G. Mazza, S. M. Giampaolo, and F. Illuminati, “Extended Bose Hubbard model of interacting bosonic atoms in optical lattices: From superfluidity to density waves,” *Phys. Rev. A* **73**, 013625 (2006).
- ⁸¹ Ulf Bissbort, Frank Deuretzbacher, and Walter Hofstetter, “Effective multibody-induced tunneling and interactions in the Bose-Hubbard model of the lowest dressed band of an optical lattice,” *Phys. Rev. A* **86**, 023617 (2012).
- ⁸² Dirk-Sören Lühmann, Ole Jürgensen, and Klaus Sengstock, “Multi-orbital and density-induced tunneling of bosons in optical lattices,” *New J. Phys.* **14**, 033021 (2012).
- ⁸³ Omjyoti Dutta, Mariusz Gajda, Philipp Hauke, Maciej Lewenstein, Dirk-Sören Lühmann, Boris A Malomed, Tomasz Sowiński, and Jakub Zakrzewski, “Non-standard Hubbard models in optical lattices: a review,” *Rep. Prog. Phys.* **78**, 066001 (2015).
- ⁸⁴ Ole Jürgensen, Florian Meinert, Manfred J. Mark, Hanns-Christoph Nägerl, and Dirk-Sören Lühmann, “Observation of density-induced tunneling,” *Phys. Rev. Lett.* **113**, 193003 (2014).
- ⁸⁵ S. Baier, M. J. Mark, D. Petter, K. Aikawa, L. Chomaz, Z. Cai, M. Baranov, P. Zoller, and F. Ferlaino, “Extended Bose-Hubbard models with ultracold magnetic atoms,” *Science* **352**, 201 (2016).
- ⁸⁶ A. Eckardt, “Colloquium: Atomic quantum gases in periodically driven optical lattices,” *Rev. Mod. Phys.* **89**, 011004 (2017).
- ⁸⁷ André Eckardt, Martin Holthaus, Hans Lignier, Alessandro Zenesini, Donatella Ciampini, Oliver Morsch, and Ennio Arimondo, “Exploring dynamic localization with a Bose-Einstein condensate,” *Phys. Rev. A* **79**, 013611 (2009).
- ⁸⁸ F. Meinert, M. J. Mark, K. Lauber, A. J. Daley, and H.-C. Nägerl, “Floquet engineering of correlated tunneling in the Bose-Hubbard model with ultracold atoms,” *Phys. Rev. Lett.* **116**, 205301 (2016).
- ⁸⁹ Hongzheng Zhao, Johannes Knolle, and Florian Mintert, “Engineered Nearest-Neighbour Interactions with Doubly Modulated Optical Lattices,” arXiv e-prints (2019), [arXiv:1908.05494 \[cond-mat.quant-gas\]](https://arxiv.org/abs/1908.05494).
- ⁹⁰ Luca Barbiero, Christian Schweizer, Monika Aidelsburger, Eugene Demler, Nathan Goldman, and Fabian Grusdt, “Coupling ultracold matter to dynamical gauge fields in optical lattices: From flux attachment to \mathbb{Z}_2 lattice gauge theories,” *Sci. Adv.* **5**, eaav7444 (2019).
- ⁹¹ Nicola Pancotti, Giacomo Giudice, J. Ignacio Cirac, Juan P. Garrahan, and Mari Carmen Bañuls, “Quantum East model: localization, non-thermal eigenstates and slow dynamics,” arXiv e-prints (2019), [arXiv:1910.06616 \[cond-mat.stat-mech\]](https://arxiv.org/abs/1910.06616).
- ⁹² Michael Schecter and Thomas Iadecola, “Many-body spectral reflection symmetry and protected infinite-temperature degeneracy,” *Phys. Rev. B* **98**, 035139 (2018).